



Penetrative and Marangoni convection in a fluid film over a phase boundary

Darish Jeswin Dhas¹, Anubhab Roy¹ and S. Toppaladoddi^{2,3,†}

¹Department of Applied Mechanics, Indian Institute of Technology Madras, Chennai 600036, India

²University of Leeds, Leeds LS2 9JT, UK

³University of Oxford, Oxford OX1 4AL, UK

(Received 25 January 2023; revised 24 October 2023; accepted 26 October 2023)

We study the effects of buoyancy, surface-tension gradients and phase boundary on the stability of a layer of water that is confined between air at the top and a layer of ice at the bottom. The temperature of the overlying air and flux condition at the free surface of the water layer are such that the layer is susceptible to both thermal and thermocapillary instabilities. We perform a linear stability analysis to identify these modes of instability and investigate the effects of the phase boundary on them. We find that with increasing thickness of the ice layer, the critical Rayleigh and Marangoni numbers for the instabilities are found to first decrease and then asymptote to constant values for ice thicknesses much larger than the thickness of the water layer. In the case of thermocapillary instability, we find that the thickness of the ice layer has negligible influence on the stability threshold for dimensionless wavenumber $k \gg 1$, and that the presence of an unstably stratified liquid layer significantly alters the stability threshold for $k = O(1)$. Furthermore, the inclusion of Marangoni stresses reduces the stability threshold of the thermal instability.

Key words: Marangoni convection, Bénard convection, solidification/melting

1. Introduction

Interactions between fluid flows and phase boundaries are key to understanding a wide range of phenomena in both the natural (Meakin & Jamtveit 2010) and engineered environments (Kurz & Fisher 1984). Such interactions occur at scales ranging from the microscopic (Wettlaufer & Worster 2006) to the macroscopic (Maslowski *et al.* 2012; Hewitt 2020), and have a controlling effect on the evolution of many systems, including the Earth's interior (Deguen, Alboussiere & Cardin 2013) and its polar regions (McPhee

† Email address for correspondence: s.toppaladoddi@leeds.ac.uk

2008; Ramudu *et al.* 2016), and the icy moons (Walker & Schmidt 2015; Soderlund *et al.* 2020), to name a few.

Fluid flows over phase boundaries are due principally to buoyancy forces generated because of thermal and/or compositional gradients during phase change (Davis, Müller & Dietsche 1984; Dietsche & Müller 1985; Huppert 1990; Wettlaufer, Worster & Huppert 1997; Worster 1997; Wykes *et al.* 2018) and/or mean shear flows (Delves 1968, 1971; Gilpin, Hirata & Cheng 1980; Coriell *et al.* 1984; Forth & Wheeler 1989; Feltham & Worster 1999; Neufeld & Wettlaufer 2008*a,b*; Bushuk *et al.* 2019), which in some cases were introduced to control morphological instabilities. However, in certain instances, when there is a free surface associated with the liquid layer, its dynamics can also play an important role in the evolution of the solid phase (Meakin & Jamtveit 2010). Here, we focus on the effects of a phase boundary on the thermal and thermocapillary instabilities associated with such a liquid layer. Specifically, we study the interplay between these two modes of instability in a film of water, which has a temperature of maximum density, overlying a layer of pure ice. Thermal instability in this case leads to penetrative convection (Veronis 1963; Toppaladoddi & Wettlaufer 2018).

Thermal instability in the presence of a phase boundary was first studied systematically by Davis *et al.* (1984) and Dietsche & Müller (1985) using weakly nonlinear stability analysis and experiments. The working fluid used in their experiments was cyclohexane, which has a linear equation of state and hence does not exhibit anomalous behaviour. A key finding of their study is that the critical Rayleigh number and wavenumber for the onset of instability first decrease monotonically with the thickness of the solid phase (scaled by the thickness of the liquid phase) and then asymptote to constant values for large values of the solid-phase thickness (Davis *et al.* 1984). Furthermore, the convection patterns (rolls, hexagons, or a combination of both), as observed on the underside of the solid phase, were also found to depend on the initial dimensionless thickness of the solid layer. More recent studies have explored these interactions in the laminar (Favier, Purseed & Duchemin 2019; Purseed *et al.* 2020; Toppaladoddi 2021) and turbulent (Esfahani *et al.* 2018; Ravichandran & Wettlaufer 2021) regimes.

The effects of a free liquid surface on phase change have been studied to understand the formation of icicles (Makkonen 1988; Szilder & Lozowski 1994; Short, Baygents & Goldstein 2006) and stalactites (Short *et al.* 2005*a*; Short, Baygents & Goldstein 2005*b*), and the rippled patterns on them (Ogawa & Furukawa 2002; Ueno 2007; Camporeale, Vesipa & Ridolfi 2017). Liquid film over an icicle aids in the transport of latent heat generated during phase change to the ambient air, whereas over a stalactite it transports CO₂ produced by the chemical reaction between water and CaCO₃. In both these cases, the shear flow is driven by gravity, and the transport across the liquid film is due only to diffusion. Similar rippled patterns have been observed on a layer of ice subjected to a shear- and buoyancy-driven turbulent flow over it in the presence of a free surface (Gilpin *et al.* 1980; Toppaladoddi & Wettlaufer 2019). Furthermore, in the presence of a free surface, gradients in surface tension make the liquid layer susceptible to stationary and oscillatory thermocapillary instabilities (Takashima 1981*a,b*).

Previous studies have also explored the effects of shear flows on phase-boundary evolution, with the experiments of Gilpin *et al.* (1980) being one of the first systematic studies. In their set-up, a turbulent shear flow of water was maintained over a layer of ice in a closed-loop water tunnel with a free surface. The temperature boundary conditions were such that the temperature far from the ice–water interface was above the melting point. A perturbation was initially introduced at the ice–water interface by melting a semi-cylindrical groove in the ice layer. Gilpin *et al.* (1980) observed that under certain conditions, this initial perturbation grew, leading to a ‘rippled’ surface, which impacted

considerably the heat flux to the ice–water interface. Although these effects were attributed solely to the mean shear flow (Gilpin *et al.* 1980), Toppaladoddi & Wettlaufer (2019), using Monin–Obukhov theory, showed that there were substantial buoyancy effects due to the anomalous behaviour of water. However, the potential effects of a free surface on the system’s dynamics remain unclear. Camporeale & Ridolfi (2012) studied a free-surface induced morphological instability of an inclined ice–water interface using a linear stability analysis, ignoring buoyancy effects in the liquid. For thin films, buoyancy effects are indeed negligible (Kalliadasis *et al.* 2011), and thermal effects influence only via interfacial effects, as was done in the linear stability analysis of Jiang, Cheng & Peng (2020) for a vertical falling film on an ice sheet. When the assumption of thin films is relaxed, buoyancy effects will have non-negligible effects. Bushuk *et al.* (2019) studied experimentally the formation of ice scallops on an inclined open-channel flow down an ice slab. In their experiments, the air temperature was maintained at 0 °C to ensure that melting happens predominantly due to heat transfer between water and ice. Suppose that the air temperature is marginally higher than the melting temperature. In that case, buoyancy effects in ice–water melting problems where a water layer overrides the ice can be significant due to the nonlinear equation of state. A 10 cm water layer overlying an ice layer with a 0.2 K temperature difference across the depth would have a Rayleigh number of $O(10^6)$, indicating the behaviour to be well into the regime of turbulent convection (Taylor & Feltham 2004).

The combined effects of the anomalous behaviour of water, the free surface and a melting bottom boundary are also potentially important in the evolution of melt ponds over sea ice, especially during the early stages of growth. Melt ponds form due to the melting of the snow layer overlying sea ice during the transition from winter to summer. This transition impacts considerably the effective albedo and thus the radiation budget in the Arctic. Surface melting of the sea ice in the Arctic region accounts for approximately 50 % of the total melted volume, with lateral and bottom melting accounting for the rest (Maykut & Perovich 1987). Hence there have been recent efforts to take the convective flow inside melt ponds into account, with Taylor & Feltham (2004) providing a heat transfer model for pond–ice systems. Subsequently, Skyllingstad & Paulson (2007) performed large-eddy simulations to study turbulent convection in various melt pond geometries. Recently, Kim *et al.* (2018) made *in situ* measurements of vertical temperature profiles inside a freshwater pond and a saline pond to understand the role of salinity on net heat fluxes. They also performed direct numerical simulations of the freshwater and saline water layers exposed to air on the top and bottom boundary maintained at the melting point, highlighting the asymmetric mode of convection due to the nonlinear equation of state. However, in these simulations, the bottom boundary was assumed to be rigid, ignoring phase change.

These studies on the flow dynamics in melt ponds are in the turbulent regime. However, to our knowledge, the problem of onset of convection in a liquid layer confined between a free surface and a phase boundary has not been explored. Hirata, Goyeau & Gobin (2012) studied the linear stability of under-ice melt ponds, focusing on the onset of convective instabilities owing to both salt and temperature stratifications. They studied a three-layer system comprising a melt pond, an ice matrix and an under-ice melt pond, and found that increasing ice layer thickness enhanced the system’s instability. However, they considered both the air–water and water–ice boundaries to be rigid. In the absence of strong temperature gradients within ice, thermal convection modifies dramatically the geometry of the phase boundary (Ravichandran & Wettlaufer 2021), and the solid phase in turn has considerable effect on the stability of the liquid layer (Davis *et al.* 1984;

Toppaladoddi & Wettlaufer 2019; Toppaladoddi 2021). Hence it is necessary to include the Stefan condition in the study of fluid flows over phase boundaries.

Some of the key questions that emerge from the studies of Gilpin *et al.* (1980) and Hirata *et al.* (2012) are the following. (i) What are the effects of a free surface on the evolution of an ice–water system? (ii) How does the system evolve in the presence of both stably and unstably stratified layers of liquid? (iii) How does the onset of penetrative convection depend on the thickness of the ice phase? The last question would be an extension to the studies of Davis *et al.* (1984) and Dietsche & Müller (1985) for a nonlinear equation of state. In the current study, we seek to understand these effects systematically by considering the linear stability of a layer of water confined between a layer of ice at the bottom and air at the top. The temperature boundary conditions are such that only convective motions can develop above the critical values of Rayleigh and Marangoni numbers. The problem set-up considered here is an idealised version of the melt pond geometry. We do not include an internal heat source and salinity effects, with the latter being more relevant to melt ponds over first-year ice (Kim *et al.* 2018), and focus solely on buoyancy effects due to variations in the temperature field.

The paper is organised as follows. The problem formulation and the equations of motion, along with the boundary conditions, are discussed in § 2. The details of the linear stability analysis and the results obtained are discussed in § 3. We then present the conclusions from our study in § 4.

2. Problem formulation

We consider a layer of water confined between a layer of ice at the bottom and a layer of air at the top, as shown in figure 1, in two dimensions. The initial thicknesses of the water and ice layers are h and d , respectively. There are two moving boundaries in the system: the air–water and ice–water interfaces. In the base state, these interfaces are flat. When small perturbations are introduced, the instantaneous locations of the ice–water and air–water interfaces are given by $\eta_1(x, t)$ and $h + \eta_2(x, t)$, respectively. The layer of air, the ice–water interface and the bottom plate are maintained at temperatures T_h , T_c and T_l , respectively, and are such that $T_h > T_c > T_l$. For simplicity, water and ice are assumed to have the same density (ρ_0) and thermal diffusivity (κ). The equation of state for water is nonlinear, and is well approximated by (Veronis 1963)

$$\rho(T_l) = \rho_0[1 - \alpha(T_l - T_m)^2], \quad (2.1)$$

where ρ_0 is the reference density, T_l is the temperature of water, T_m is the temperature of maximum density, and α is the coefficient of thermal expansion. This density profile has a maximum ($= \rho_0$) at $T_l = T_m$. If $T_h > T_m$, then there is a layer of stably stratified fluid overlying a layer of unstably stratified fluid (see figure 2). It is also evident from figure 2 that the depths of the stable and unstable layers are dependent on the values of T_h and T_m . With increasing values of T_h , the depth of the stably stratified layer increases. Table 1 lists the values of the relevant physical parameters for an ice–water system. In the following, we discuss the equations of motion for the different parts of the domain.

2.1. Water

The dynamics in the water layer is described by the continuity, momentum balance and heat balance equations, which are obtained after making the Boussinesq approximation

Fluid film over a phase boundary

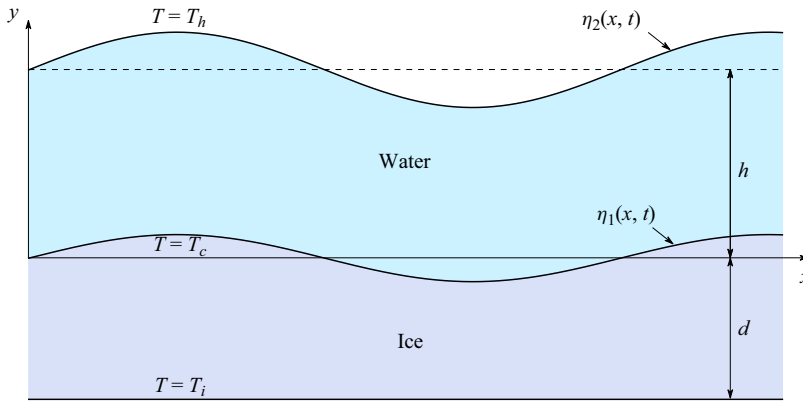


Figure 1. Schematic of a film of water over an ice sheet. The deformations in the ice–water and air–water interfaces are exaggerated for better illustration.

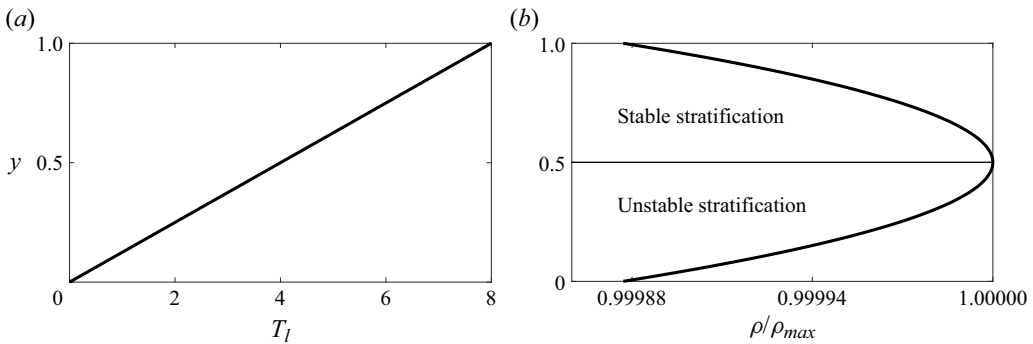


Figure 2. Base state (a) temperature and (b) density profiles of the liquid layer drawn with $T_h = 8^\circ\text{C}$, $T_c = 0^\circ\text{C}$ and $T_m = 4^\circ\text{C}$, and the corresponding density profile obtained using (2.1). Plot (b) also shows the regions of stable and unstable density stratification.

Parameter	Value
Density, ρ (kg m^{-3})	10^3
Surface tension, σ_0 (kg s^{-2})	7.49×10^{-2}
Surface tension gradient, γ ($\text{kg s}^{-2} \text{K}^{-1}$)	0.14×10^{-3}
Kinematic viscosity, ν ($\text{m}^2 \text{s}^{-1}$)	1.5705×10^{-6}
Latent heat, L_s (J kg^{-1})	3.334×10^5
Specific heat, c_p ($\text{J kg}^{-1} \text{K}^{-1}$)	4200
Thermal diffusivity, κ ($\text{m}^2 \text{s}^{-1}$)	1.35×10^{-7}
Thermal conductivity, \mathcal{K} ($\text{J m}^{-1} \text{s}^{-1} \text{K}^{-1}$)	0.561
Coefficient of thermal expansion, α ($^\circ\text{C}^{-2}$)	7.68×10^{-6}
Heat transfer coefficient, χ ($\text{W m}^{-2} \text{K}^{-1}$)	1000
Acceleration due to gravity, g ($\text{m}^2 \text{s}^{-1}$)	9.81
Temperature of maximum density, T_m ($^\circ\text{C}$)	4
Temperature of ice–water interface, T_c ($^\circ\text{C}$)	0
Temperature of air–water interface, T_h ($^\circ\text{C}$)	8
Temperature of bottom plate, T_i ($^\circ\text{C}$)	–1

Table 1. Estimates of physical parameters for an ice–water–air system at 277 K.

and are given by (Chandrasekhar 2013)

$$\nabla \cdot \mathbf{u} = 0, \tag{2.2}$$

$$\frac{\partial \mathbf{u}}{\partial t} + \mathbf{u} \cdot \nabla \mathbf{u} = -\frac{1}{\rho_0} \nabla P + \nu \nabla^2 \mathbf{u} + [1 - \alpha(T_l - T_m)^2] \mathbf{g} \tag{2.3}$$

and

$$\frac{\partial T_l}{\partial t} + \mathbf{u} \cdot \nabla T_l = \kappa \nabla^2 T_l. \tag{2.4}$$

Here, $\mathbf{u} = (u, v)$ is the velocity field, ν is the kinematic viscosity, P is the pressure field, and \mathbf{g} is the acceleration due to gravity.

2.2. Ice

In the ice layer, the temperature field T_s is governed by the diffusion equation:

$$\frac{\partial T_s}{\partial t} = \kappa \nabla^2 T_s. \tag{2.5}$$

2.3. Ice–water interface

The dynamics of the ice–water interface is governed by the Stefan condition, which – for small amplitudes of interfacial deformation – is given by

$$\rho_0 L_s \frac{\partial \eta_1}{\partial t} = \mathbf{n} \cdot [\mathbf{q}_l - \mathbf{q}_s]_{y=\eta_1}. \tag{2.6}$$

Here, L_s is the latent heat of fusion, \mathbf{q}_s and \mathbf{q}_l are the conductive heat fluxes into the ice from the interface and from the water layer towards the interface, respectively, and \mathbf{n} is the outward unit normal at the interface, given by

$$\mathbf{n} = \frac{1}{\sqrt{1 + (\partial \eta_1 / \partial x)^2}} \left(-\frac{\partial \eta_1}{\partial x}, 1 \right). \tag{2.7}$$

2.4. Boundary conditions

We impose the following boundary conditions at the different interfaces.

- (i) The temperature boundary condition at the bottom plate ($y = -d$) is given by

$$T_s = T_i. \tag{2.8}$$

- (ii) The velocity and temperature boundary conditions at the ice–water interface ($y = \eta_1(x, t)$) are

$$\mathbf{u} \cdot \mathbf{n} = \mathbf{u} \cdot \mathbf{t} = 0, \tag{2.9}$$

$$T_s = T_l = T_c. \tag{2.10}$$

Here, \mathbf{t} is the unit tangent at the interface.

- (iii) The balances of normal and tangential stresses at the air–water interface ($y = h + \eta_2(x, t)$) are

$$P = \frac{2\mu}{\left[1 + \left(\frac{\partial\eta_2}{\partial x}\right)^2\right]} \left[\frac{\partial u}{\partial x} \left(\frac{\partial\eta_2}{\partial x}\right)^2 - \left(\frac{\partial v}{\partial x} + \frac{\partial u}{\partial y}\right) \frac{\partial\eta_2}{\partial x} + \frac{\partial v}{\partial y} \right] - \frac{\sigma \frac{\partial^2\eta_2}{\partial x^2}}{\left[1 + \left(\frac{\partial\eta_2}{\partial x}\right)^2\right]^{3/2}}, \quad (2.11)$$

$$\begin{aligned} & \mu \left[4 \frac{\partial u}{\partial x} \frac{\partial\eta_2}{\partial x} - \left(1 - \left(\frac{\partial\eta_2}{\partial x}\right)^2\right) \left(\frac{\partial u}{\partial y} + \frac{\partial v}{\partial x}\right) \right] \\ & = \gamma \left(\frac{\partial\eta_2}{\partial x} \frac{\partial T_l}{\partial y} + \frac{\partial T_l}{\partial x}\right) \sqrt{1 + \left(\frac{\partial\eta_2}{\partial x}\right)^2}. \end{aligned} \quad (2.12)$$

Here, $\sigma = \sigma_0 - \gamma(T_l - T_h)$ is the surface tension, and $\gamma = -(d\sigma/dT)|_{T_a}$.

- (iv) At the air–water interface ($y = h_0 + \eta_2(x, t)$), we consider Newton’s law of cooling:

$$\mathcal{K}\mathbf{n} \cdot \nabla T_l = -\chi(T_l - T_h). \quad (2.13)$$

Here, \mathcal{K} is the thermal conductivity of water, and χ is the heat transfer coefficient. A discussion of the above imperfect heat transfer between the overlying air and the underlying phase can be found in Hitchen & Wells (2016). Although Hitchen & Wells (2016) derived the boundary condition in the context of sea ice growth, it remains valid as a model for the interface of a melt pond (Kim *et al.* 2018).

- (v) The kinematic boundary condition at the air–water interface ($y = h_0 + \eta_2(x, t)$) is

$$\frac{\partial\eta_2}{\partial t} + u \frac{\partial\eta_2}{\partial x} = v. \quad (2.14)$$

The above system of equations is made dimensionless using the height h as the length scale, $u_0 = \kappa/h$ as the velocity scale, $P_0 = \rho\nu\kappa/h^2$ as the pressure scale, and $\Delta T = T_h - T_c$ as the temperature scale. With the Rayleigh number as $Ra = gh^3\alpha \Delta T^2/(\nu\kappa)$, the capillary number as $Ca = \rho\nu\kappa/(\sigma_0h)$, the Marangoni number as $Ma = \gamma \Delta T h/(\rho\nu\kappa)$, the Prandtl number as $Pr = \nu/\kappa$, the Stefan number as $\mathcal{S} = L_s/(c_p \Delta T)$, the Biot number as $Bi = \chi h/K$, $\lambda = \Delta T/(T_m - T_c)$ and $\zeta = \alpha(\lambda(T_m - T_c))^2$, the dimensionless equations are given by

$$\nabla \cdot \mathbf{u} = 0, \quad (2.15)$$

$$\frac{\partial \mathbf{u}}{\partial t} + \mathbf{u} \cdot \nabla \mathbf{u} = Pr [-\nabla P + \nabla^2 \mathbf{u} - Ra (\zeta^{-1} - \theta_l^2) \mathbf{y}], \quad (2.16)$$

$$\frac{\partial \theta_l}{\partial t} + \mathbf{u} \cdot \nabla \theta_l = \nabla^2 \theta_l, \quad (2.17)$$

$$\frac{\partial \theta_s}{\partial t} = \nabla^2 \theta_s, \quad (2.18)$$

and the dimensionless boundary conditions are:

(i) at $y = -d/h$,

$$\theta_s = \theta_i; \tag{2.19}$$

(ii) at $y = \eta_1$,

$$u = v = 0, \tag{2.20}$$

$$\theta_s = \theta_l = \theta_c, \tag{2.21}$$

$$\frac{\partial \eta_1}{\partial t} = -\frac{1}{S\sqrt{1 + \left(\frac{\partial \eta_2}{\partial x}\right)^2}} \left\{ \frac{\partial}{\partial y}(\theta_l - \theta_s) - \frac{\partial \eta_1}{\partial x} \frac{\partial}{\partial x}(\theta_l - \theta_s) \right\}; \tag{2.22}$$

(iii) at $y = 1 + \eta_2$,

$$P = \frac{2}{\left[1 + \left(\frac{\partial \eta_2}{\partial x}\right)^2\right]} \left[\frac{\partial u}{\partial x} \left(\frac{\partial \eta_2}{\partial x}\right)^2 - \left(\frac{\partial v}{\partial x} + \frac{\partial u}{\partial y}\right) \frac{\partial \eta_2}{\partial x} + \frac{\partial v}{\partial y} \right] - \frac{[Ca^{-1} + Ma(\theta_l - \theta_h)] \frac{\partial^2 \eta_2}{\partial x^2}}{\left[1 + \left(\frac{\partial \eta_2}{\partial x}\right)^2\right]^{3/2}}, \tag{2.23}$$

$$4 \frac{\partial u}{\partial x} \frac{\partial \eta_2}{\partial x} - \left(1 - \left(\frac{\partial \eta_2}{\partial x}\right)^2\right) \left(\frac{\partial u}{\partial y} + \frac{\partial v}{\partial x}\right) = -Ma \left(\frac{\partial \eta_2}{\partial x} \frac{\partial \theta_l}{\partial y} + \frac{\partial \theta_l}{\partial x}\right) \sqrt{1 + \left(\frac{\partial \eta_2}{\partial x}\right)^2}, \tag{2.24}$$

$$\frac{1}{\sqrt{1 + \left(\frac{\partial \eta_2}{\partial x}\right)^2}} \left\{ \frac{\partial \theta_l}{\partial y} - \frac{\partial \eta_2}{\partial x} \frac{\partial \theta_l}{\partial x} \right\} = -Bi(\theta_l - \theta_h), \tag{2.25}$$

$$\frac{\partial \eta_2}{\partial t} + u \frac{\partial \eta_2}{\partial x} = v. \tag{2.26}$$

Here, $\theta_l = (T_l - T_m)/\Delta T$, $\theta_c = (T_c - T_m)/\Delta T$, $\theta_s = (T_s - T_m)/\Delta T$ and $\theta_i = (T_i - T_m)/\Delta T$.

The parameter λ , as defined by Veronis (1963), is the ratio between the total depth of the liquid layer and the depth of the unstably stratified layer of the liquid, and is equivalent to the definition used here in the $Bi \rightarrow \infty$ limit. For water, $T_c = 0^\circ\text{C}$ and $T_m = 4^\circ\text{C}$, thus $T_h = 4\lambda^\circ\text{C}$. Additionally, we also have the Galilei number, defined as $Ga = Ra/\zeta = gh^3/(\nu\kappa)$ (Velarde, Nepomnyashchy & Hennenberg 2001; Lyubimov *et al.* 2018). However, since Ga cannot be varied independently, we choose not to include it explicitly in our equations. Figure 3 shows the values of the mentioned non-dimensional numbers as functions of the film height.

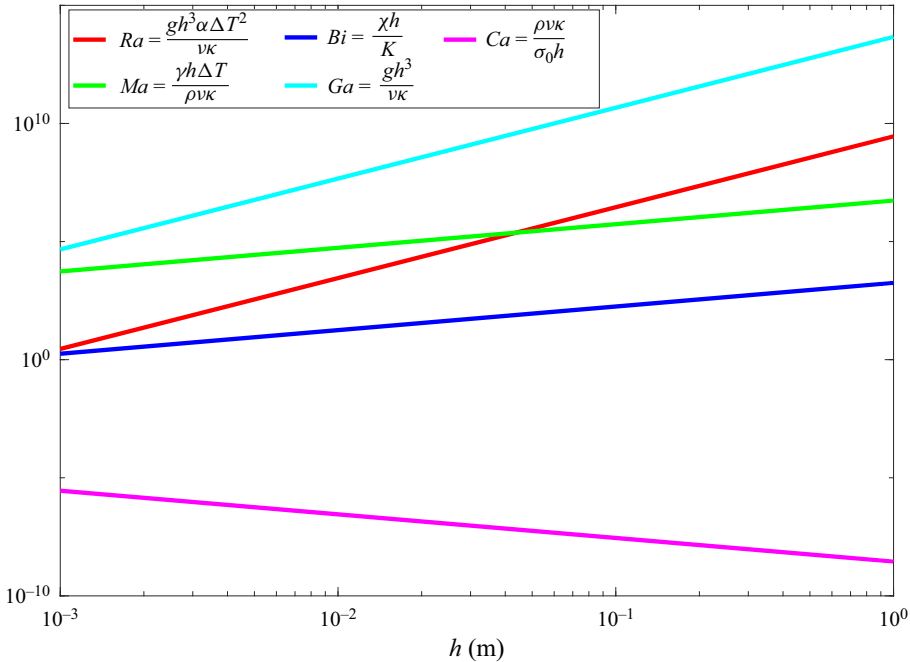


Figure 3. Non-dimensional numbers plotted for a range of film height h with $\Delta T = 8^\circ\text{C}$ using the physical parameters listed in table 1.

3. Linear stability analysis

In the base state, there are no fluid motions, and the air–water and ice–water interfaces are planar. The base-state temperature fields in the ice and water layers are obtained by solving the steady-state diffusion equation, and the solutions are given by

$$\theta_s^b = \theta_c + \frac{\theta_c - \theta_i}{d/h} y, \quad (3.1)$$

$$\theta_l^b = \theta_c + \frac{Bi}{1 + Bi} y, \quad (3.2)$$

where the superscript b denotes base state. In order for the ice–water interface to remain planar and fixed in the base state, we require that the heat fluxes at the interface balance. This leads to

$$\frac{\theta_c - \theta_i}{d/h} = \frac{Bi}{1 + Bi}. \quad (3.3)$$

We now introduce normal-mode perturbations in the system with wavenumber k and wave speed c . As a result of this, each physical parameter in the system (say X) is given by $X(x, y, t) = X^b(x) + \hat{X}(y) \exp(ik(x - ct))$, with X^b denoting the base-state value, and \hat{X} denoting the infinitesimally small amplitude of the disturbance ($|\hat{X}| \ll |X^b|$). Linearising (2.15)–(2.18) about the base state, we get

$$\{Pr(\mathcal{D}^2 - k^2)^2 + ikc(\mathcal{D}^2 - k^2)\} \hat{v} - \{2k^2 Ra Pr \theta_l^b\} \hat{\theta}_l = 0, \quad (3.4)$$

$$\{\mathcal{D}^2 - k^2 + ikc\}\hat{\theta}_l - \left\{\frac{d\theta_l^b}{dy}\right\}\hat{v} = 0, \tag{3.5}$$

$$\{\mathcal{D}^2 - k^2\}\hat{\theta}_s = -ikc\hat{\theta}_s, \tag{3.6}$$

with boundary conditions at $y = -d/h$

$$\hat{\theta}_s = 0, \tag{3.7}$$

at $y = 0$

$$\mathcal{D}\hat{v} = 0, \tag{3.8}$$

$$\hat{v} = 0, \tag{3.9}$$

$$\frac{d\theta_s^b}{dy}\hat{\eta}_1 + \hat{\theta}_s = 0, \tag{3.10}$$

$$\frac{d\theta_l^b}{dy}\hat{\eta}_1 + \hat{\theta}_l = 0, \tag{3.11}$$

$$\mathcal{D}\hat{\theta}_l - \mathcal{D}\hat{\theta}_s = ikcS\hat{\eta}_1, \tag{3.12}$$

and at $y = 1$

$$(\mathcal{D}^2 + k^2)\hat{v} = k^2 Ma \left(\frac{d\theta_l^b}{dy}\eta_2 + \hat{\theta}_l\right), \tag{3.13}$$

$$\{ikc\mathcal{D} + Pr(\mathcal{D}^2 - 3k^2)\mathcal{D}\}\hat{v} - Prk^2\{Ra(\zeta^{-1} - (\theta_l^b)^2) + k^2[Ca^{-1} + Ma(\theta_l^b - \theta_h)]\}\hat{\eta}_2 = 0, \tag{3.14}$$

$$ikc\hat{\eta}_2 + \hat{v} = 0, \tag{3.15}$$

$$(\mathcal{D} + Bi)\hat{\theta}_l + Bi\frac{d\theta_l^b}{dy}\hat{\eta}_2 = 0. \tag{3.16}$$

Here, \mathcal{D} denotes the derivative of the perturbation amplitudes with respect to y . The above system of linear equations is similar to the corresponding system obtained for a flow between two parallel plates with a stress-free surface, first derived by Veronis (1963) without the ice layer. The full system of linear equations (3.4)–(3.16) does not admit an analytical solution. However, as the perturbation temperature field in the ice layer is decoupled from the momentum and temperature perturbation fields in the fluid layer, the analytical solution to (3.6), subject to boundary conditions (3.7) and (3.10), is found to be

$$\hat{\theta}_s = a_1 \exp(\sqrt{k(k-ic)}y) + a_2 \exp(-\sqrt{k(k-ic)}y), \tag{3.17}$$

$$a_1 = -\frac{Bi}{1+Bi}\hat{\eta}_1 \frac{\exp(2\sqrt{k(k-ic)}d/h)}{\exp(2\sqrt{k(k-ic)}d/h) - 1}, \tag{3.18}$$

$$a_2 = \frac{Bi}{1+Bi}\hat{\eta}_1 \frac{1}{\exp(2\sqrt{k(k-ic)}d/h) - 1}. \tag{3.19}$$

3.1. Results

We now study the coupling between thermocapillary and thermal instabilities, and the impact of the phase boundary on them, by solving the linearised equations (3.4)–(3.6), along with the boundary conditions (3.7)–(3.16).

3.1.1. Thermocapillary instability

We first wish to understand the effects of convective motions on the thermocapillary instability. To this end, we follow Takashima (1981a) and study the thermocapillary instability in the limit of small wavenumbers ($k \ll 1$). By expanding the perturbative quantities in (3.4)–(3.16) in powers of k , and solving the equations to $O(k)$, we obtain the complex wave speed as

$$\begin{aligned}
 c &= c_0 + kc_1 + O(k^2) \\
 &\approx \frac{1}{\eta_{20}} \int_0^1 \hat{u}_0 \, dy + ik \frac{1}{\eta_{20}} \int_0^1 \left(\hat{u}_1 - \frac{\eta_{21}}{\eta_{20}} \hat{u}_0 \right) \, dy \\
 &\approx ik \left\{ \left(\frac{Bi}{1 + Bi} \right)^2 \frac{Ra (60 + Bi (34 + 27d/h))}{180(1 + Bi + Bi d/h)} + \frac{Bi}{1 + Bi} \frac{Ra \theta_c (40 + Bi (29 + 25d/h))}{60(1 + Bi + Bi d/h)} \right. \\
 &\quad \left. + \frac{Ra \theta_c^2}{3} - \frac{Ga}{3} + \frac{Bi}{(1 + Bi + Bi d/h)(1 + Bi)} \frac{Ma}{2} \right\}. \tag{3.20}
 \end{aligned}$$

We should note that solutions to the linearised system (3.4)–(3.16) appear only at even powers of k . This becomes apparent if we replace kc with ω , which results in k appearing solely at even powers (implying $c = kc_1 + k^3c_3 + O(k^5)$) and is due to the absence of a background flow. However, in the presence of a background flow, $c_0 \neq 0$, as in the case of falling films (Yih 1963; Dhas & Roy 2022). For brevity, we have not included the expression for the $O(k^3)$ correction to the wave speed here (see figure 5 for comparisons against the wave speed obtained numerically). The critical Marangoni number Ma_c is obtained subsequently by setting $c = 0$ in the above equation, giving

$$\begin{aligned}
 Ma_c \approx & \frac{(1 + Bi + Bi d/h)(1 + Bi)}{Bi} \left(\frac{2 Ga}{3} - \frac{2 Ra \theta_c^2}{3} \right) \\
 & - \frac{Bi Ra (60 + Bi (34 + 27d/h))}{90(1 + Bi)} - \frac{Ra \theta_c (40 + Bi (29 + 25d/h))}{30}. \tag{3.21}
 \end{aligned}$$

If we ignore buoyancy and the phase boundary (by setting $d/h = 0$), impose an adiabatic boundary condition at the air–water surface in the base state, and set $\theta_c = -1$ (which corresponds to the case where $T_m = T_h$), then the critical Marangoni number becomes

$$Ma_c = \frac{2}{3} Ga (1 + Bi). \tag{3.22}$$

The above expression is consistent with the result obtained by Takashima (1981a), thereby demonstrating that our general expression for Ma_c reduces to this special case. An important implication of result (3.21) is that for $k \ll 1$, Ma_c is independent of the equation of state of the fluid, and is the same for both linear and nonlinear equations of state. This is also evident from (3.4), where the buoyancy term is $O(k^2)$. We will use this result to discern the effects of penetrative convection on Ma_c . We note that we are

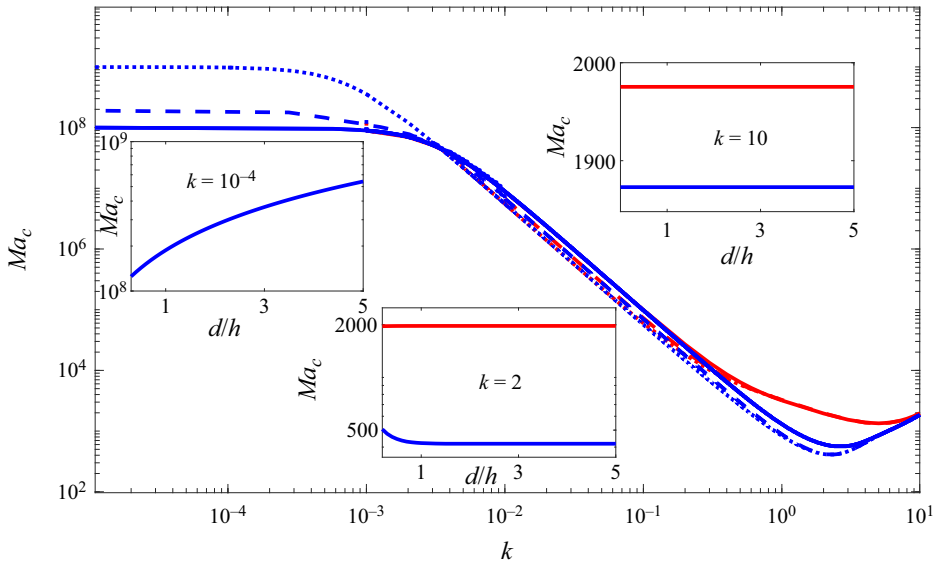


Figure 4. Neutral stability curves drawn in the Ma_c - k plane for $d/h = 0$ (solid lines), $d/h = 1$ (dashed lines) and $d/h = 10$ (dotted lines) with a linear equation of state (red lines) and a nonlinear equation of state (blue lines). The insets depict neutral curves in the Ma_c - d/h plane for wavenumbers $k = 10^{-4}$, 2 and 10, and $Ra = 6000$. The region above the curves is the zone of instability.

interested in the marginal states of the stationary thermocapillary instability, wherein both the real and imaginary parts of the wave speed c would be zero. This implies that the small deformations of both the phase boundary and the free surface do not affect the condition for marginal stability as a consequence of the linearisation (see (3.12) and (3.15)).

The equations corresponding to the nonlinear equation of state (3.4)–(3.6), do not admit analytical solutions, but the corresponding equations with a linear equation of state do. Therefore, we first study the system corresponding to the linear equation of state. Note that since we are looking at a system that is hot on top and cold at the bottom, onset of thermal instability is not possible when using a linear equation of state. (Details on the calculations corresponding to the linear equation of state can be found in Appendix A.) We assign the values of the parameters as $Pr = 11.6$, $\lambda = 2$, $\mathcal{S} = 10$, $Ca = 10^{-6}$ and $Bi = 10$ for all of our subsequent calculations, unless specified otherwise. We also choose the value of Ra as 6000 to study the thermocapillary instability such that it lies below the critical threshold corresponding to the thermal instability mode for $Ma = 0$ (see § 3.1.2).

In figure 4, we show the neutral stability curves for $d/h = 0$ (implying the absence of an ice layer), $d/h = 1$ and $d/h = 10$ calculated using the linear equation of state (red curves). It is seen that for a fixed value of d/h , the critical Marangoni number decreases with increasing k . The criticality threshold decreases until we reach $k = O(1)$. This is again consistent with the results of Takashima (1981a). The insets in figure 4 show Ma_c as a function of d/h for different fixed values of k . For $k \ll 1$, Ma_c increases monotonically with increasing d/h . However, for $k = O(1)$ and $k \gg 1$, Ma_c is independent of d/h . Hence the effects of phase boundary on the thermocapillary instability for $k = O(1)$ and $k \gg 1$ are qualitatively similar to its effects on Rayleigh–Bénard convection (Davis *et al.* 1984).

Having explored the thermocapillary instability in the absence of penetrative convection, we now study the effects of a nonlinear equation of state by solving (3.4)–(3.5) numerically using the Chebyshev spectral collocation method (Trefethen 2000). (Further

$\lambda = \Delta T / (T_m - T_c)$	Numerical results – Veronis (1963)		Numerical results – present work	
	Ra_c	k_c	Ra_c	k_c
2	1.868×10^4	4	18 663	4
2.5	4.629×10^4	5.06	46 286	5.1
3	9.558×10^4	6.1	95 571	6.1
3.5	1.771×10^5	7.1	177 043	7.1

Table 2. Comparisons for validation of the stability code with the results by Veronis (1963) for the rigid boundary case.

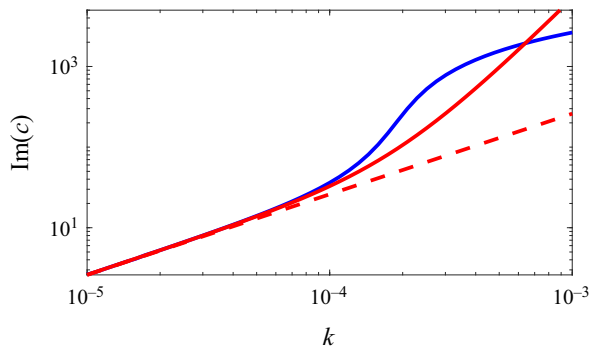


Figure 5. The imaginary part of the wave speed $\text{Im}(c)$ associated with the thermocapillary instability mode obtained numerically (blue line), from the $O(k^3)$ long-wave calculation (red solid line) and from the $O(k)$ long-wave expression in (3.20) (red dashed line). Here, $Ra = 6000$, $Ma = 2 \times 10^8$, $\lambda = 2$, $S = 10$ and $Bi = 10$.

details of the numerical method used are provided in Appendix B.) To validate our numerical code, we reproduce the results of Veronis (1963) for penetrative convection with the top and bottom boundaries being rigid. The results from this validation are shown in table 2, and are in good agreement. Further, we also compare the wave speed obtained numerically with the long-wave analytical calculation. We obtain excellent agreement in the long-wave limit ($k \ll 1$) between the analytical and numerical calculations, as shown in figure 5.

The marginal stability curves for the case of the nonlinear equation of state (in blue) are shown in figure 4. Comparing the Ma_c values for the linear and the nonlinear equations of state, we see that there is negligible difference between them for $k < O(1)$ (compare the blue and red lines in figure 4, and the inset for $k = 10^{-4}$). The same can be said for $k \gg 1$ (see the inset for $k = 10$ in figure 4). However, for $k = O(1)$, the values of Ma_c in the presence of penetrative convection are significantly lower than those in the absence of convective motions (see the inset for $k = 2$ in figure 4).

The reason for this difference in behaviour can be seen by studying the eigenfunctions of the temperature disturbance, which are shown in figure 6. We see from these images that for $k = 10^{-4}$ and $k = 10$, there is no discernible difference between the temperature fields in the presence and absence of penetrative convection. In both cases, the temperature perturbations are mostly confined near the air–water interface. However, for $k = O(1)$, here represented with $k = 2$, we see that the Bénard cells penetrate significantly deeper in the presence of penetrative convection. These findings corroborate what we observed

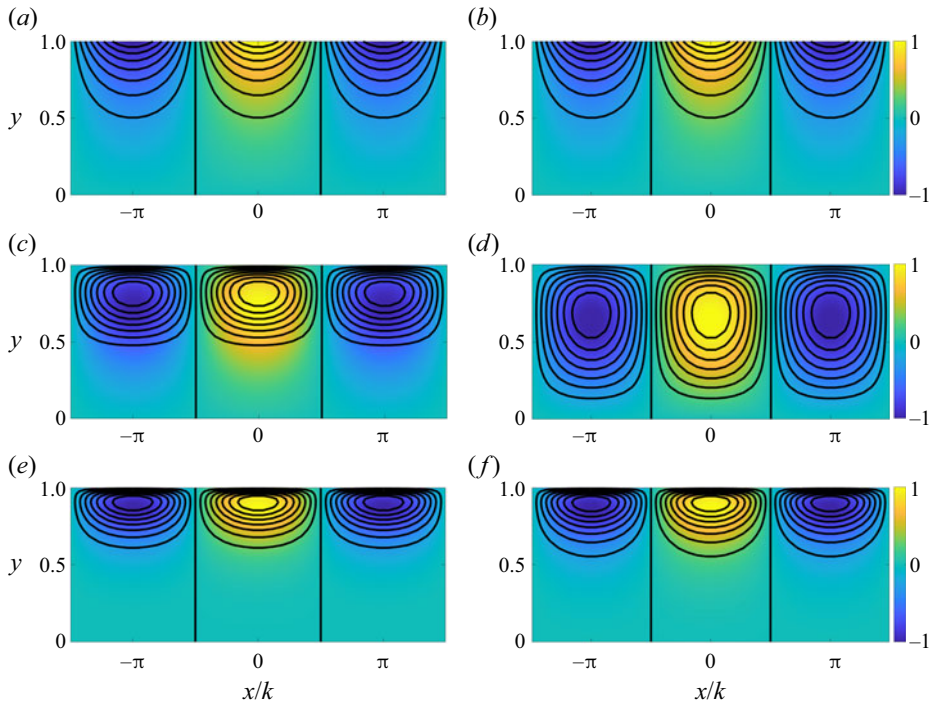


Figure 6. Perturbed temperature field with the streamfunction plotted for $d/h = 0.1$ and $Ra = 6000$. The values chosen for Ma are greater than the corresponding Ma_c . (a) Linear equation of state, $k = 10^{-4}$, $Ma = 10^9$. (b) Nonlinear equation of state, $k = 10^{-4}$, $Ma = 10^9$. (c) Linear equation of state, $k = 2$, $Ma = 2000$. (d) Nonlinear equation of state, $k = 2$, $Ma = 2000$. (e) Linear equation of state, $k = 10$, $Ma = 2000$. (f) Nonlinear equation of state, $k = 10$, $Ma = 2000$.

previously with the neutral stability curves in figure 4. It is clear from these results that the coupling between penetrative convection and the thermocapillary instability is established through the disturbance wavenumber. For $k \ll 1$, the effects of buoyancy are not felt; and for $k \gg 1$, the disturbances are confined to a region close to the air–water interface. However, only for $k = O(1)$ do the disturbances penetrate into the unstably stratified region. When $\Delta T = 8$, the upper half of the fluid layer is stably stratified and the lower half is unstably stratified. Hence disturbances with $k = O(1)$ are of wavelengths comparable to the thickness of the liquid layer and therefore get stretched when they encounter the unstably stratified region.

The results shown in figure 4 were obtained for $Ra < Ra_c$ in a corresponding system devoid of thermal effects (see § 3.1.2 for details on the thermal instability mode). We next probe the thermocapillary instability for $Ra = 20\,000$, such that both the thermocapillary and thermal instabilities can coexist. The results for such a case are shown in the black curves of figure 7. We find that this higher value of Ra is stabilising for $k \ll 1$, whereas it is destabilising for $k = O(1)$. This destabilisation is due to the emergence of the thermal mode of instability. Yet another aspect is the influence of the depth of penetrative convection dictated by the parameter $\lambda = 2$. Decreasing the value of λ increases the depth of the unstable layer, thereby potentially lowering the critical Rayleigh number for the thermal mode of instability. Therefore, as expected, we observe similar trends for the cases $\lambda = 1.5$ and 0.5 as with the case $Ra = 20\,000$ – stabilising for small values of the wavenumber, and destabilising for $O(1)$ values of the wavenumber. For $\lambda = 0.5$ ($T_h = 2$),

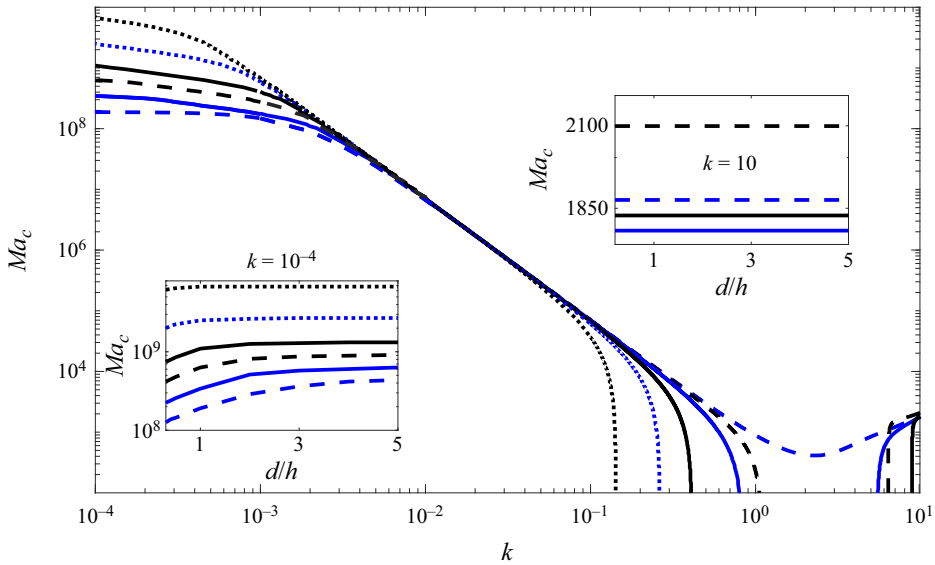


Figure 7. Neutral stability curves drawn in the Ma_c - k plane for $d/h = 1$, $\lambda = 2$ (dashed lines), $\lambda = 1.5$ (solid lines) and $\lambda = 0.5$ (dotted lines), with $Ra = 6000$ (blue) and $Ra = 20000$ (black), with a nonlinear equation of state. The insets depict neutral curves in the Ma_c - d/h plane for wavenumbers $k = 10^{-4}$ and 10. The region above the curves is the zone of instability.

no penetrative convection exists since the water layer is unstably stratified along its entire depth. The lack of any critical Marangoni number in the region of $O(1)$ wavenumbers in figure 7 is due to the thermal mode of instability taking over to destabilise the system. We note that for $\lambda = 1.5$ and 0.5 , the critical Rayleigh number corresponding to the thermal instability mode is lower than 6000. Further details on the thermal instability mode are provided in § 3.1.2.

In addition to the effects of the nonlinear equation of state, we also explore the impact of the Stefan number (\mathcal{S}) on the thermocapillary instability. Figure 8 shows the neutral stability curves plotted for $\mathcal{S} = 1$ and 10. From (3.12), it is clear that variations in \mathcal{S} will not have any impact on the stability threshold associated with the stationary thermocapillary instability mode being studied here. This is because \mathcal{S} drops out of (3.12), since the wave speed is zero at the marginal states of the stationary instability mode. However, $\text{Re}(c) \neq 0$ for the oscillatory instability mode. Therefore, we probe the influence of Stefan number by computing the neutral curves for the oscillatory instability (see the inset in figure 8). We find that the region of instability expands with an increase in Stefan number from $\mathcal{S} = 1$ to $\mathcal{S} = 10$. We also find the instability region expands significantly with an increase in thickness of the ice layer. Despite this, it is important to note that the oscillatory instability is not particularly relevant to ice–water systems since we find that it is triggered only at Marangoni numbers of $O(10^8)$ or higher. Such Marangoni numbers are associated with water layers that are a few metres in thickness (see figure 3). Regnier, Dauby & Lebon (2000), in their analysis, also note that the oscillatory thermocapillary instability is not possible under realistic conditions on Earth under the Boussinesq approximation. Therefore, we restrict the study of the oscillatory thermocapillary instability only to highlight the influence of the Stefan number. As expected, we find no perceivable change in the critical Marangoni numbers corresponding to the stationary thermocapillary instability.

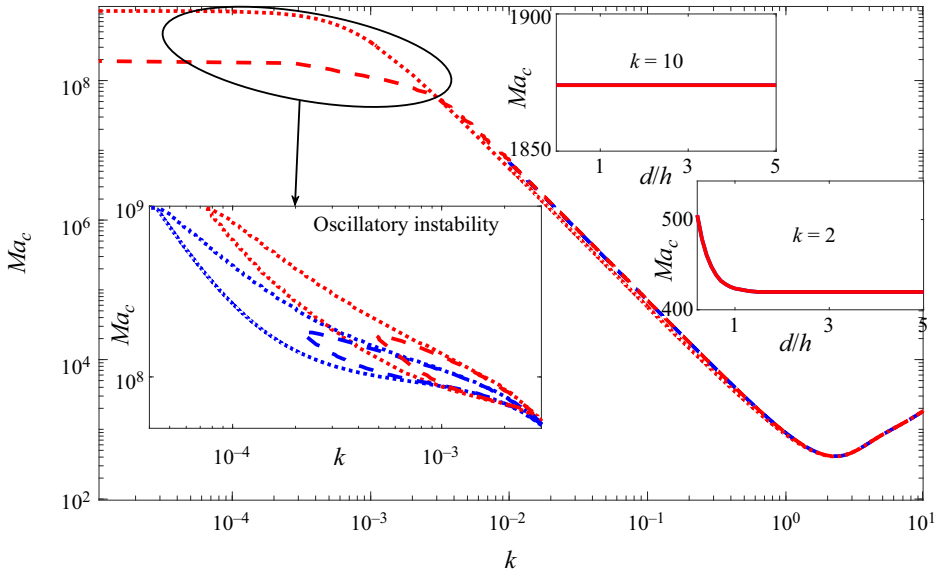


Figure 8. Neutral stability curves drawn in the Ma_c - k plane for $d/h = 1$ (dashed lines) and $d/h = 10$ (dotted lines), with $\mathcal{S} = 10$ (blue) and $\mathcal{S} = 1$ (red), with a nonlinear equation of state. The bottom left inset shows the oscillatory thermocapillary instability, for which the region enclosed by the curves is unstable. The other insets depict neutral curves in the Ma_c - d/h plane for wavenumbers $k = 2$ and 10 , and $Ra = 6000$.

3.1.2. Thermal instability

The Marangoni stresses are not the only source of instability in this system. As noted previously, due to the anomalous behaviour of water, we have a base state in which a part of the liquid layer is unstably stratified. We now study this thermal mode of instability in the absence of Marangoni stresses ($Ma = 0$). In figures 9(a) and 9(b), the dependence of the critical Rayleigh number Ra_c and critical wavenumber k_c on d/h is shown for $Bi = 10$ and 100 . For a fixed value of Bi , we find that both Ra_c and k_c first decrease with increasing d/h , and then asymptote to constant values ($Ra_c \approx 10\,248$, $k_c \approx 2.85$ for $Bi = 10$, and $Ra_c \approx 13\,840$, $k_c \approx 3.3$ for $Bi = 100$). Thus we find that the presence of the phase boundary has a destabilising effect. This is again qualitatively consistent with the results of Davis *et al.* (1984) for Rayleigh–Bénard convection over a phase boundary. The reason for this destabilising effect is that in the limit $d/h \rightarrow 0$, the ice layer becomes a perfect conductor, and the classical case is recovered. However, in the opposite limit, $d/h \rightarrow \infty$, the ice layer becomes a poor conductor and more susceptible to deformations, and hence less stable (Davis *et al.* 1984).

Between the two values of Bi studied, we find that the higher value yields more stability (see figure 9a). The reason for this is the following. When the free surface is insulated ($Bi = 0$), temperature perturbations are easier to set up. However, when the free surface can convect heat, as would be the case for large Bi , any temperature perturbations introduced would decay (Nield 1964). This is evident from the thermal boundary condition prescribed at the free surface (see (3.16)). Thus larger values of the temperature gradient are required to destabilise the system for increasing values of Bi (Nield 1964).

We next study the influence of the depth of penetrative convection on the system’s stability. Figures 10(a) and 10(b) show the critical Rayleigh number and wavenumber, respectively, for three values of λ , namely 0.5, 1.5 and 2. We find that in the cases

Fluid film over a phase boundary

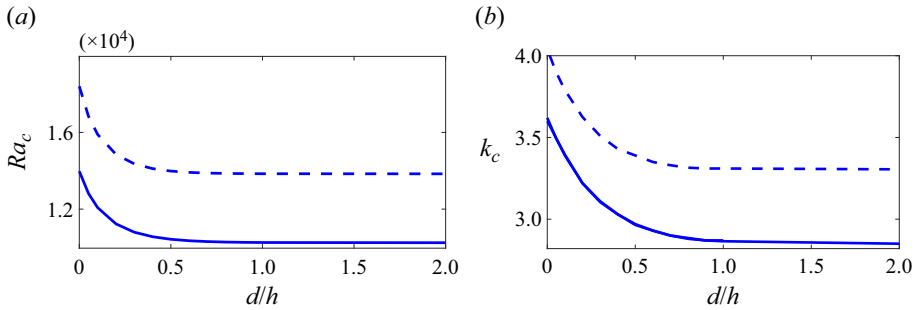


Figure 9. Neutral stability curves for Biot numbers $Bi = 10$ (solid lines) and $Bi = 100$ (dashed lines), with $Ma = 0$. The region above the curves is the zone of instability.

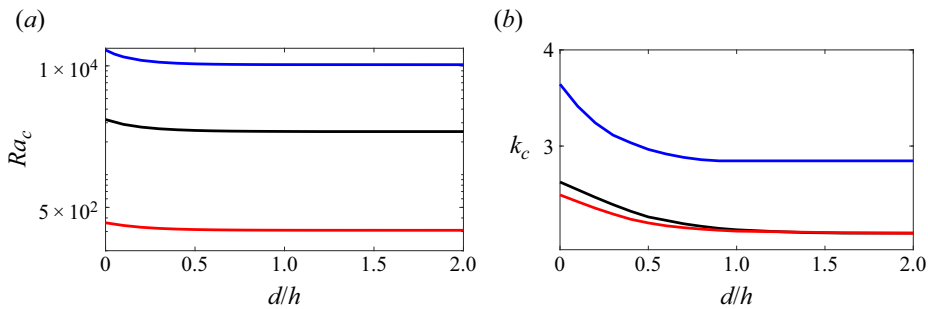


Figure 10. Neutral stability curves for $\lambda = 0.5$ (red), $\lambda = 1.5$ (black) and $\lambda = 2$ (blue), with $Bi = 10$ and $Ma = 0$. The region above the curves is the zone of instability.

$\lambda = 0.5$ and 1.5 , the stability thresholds drop significantly in comparison to the case $\lambda = 2$, throughout the range of d/h explored. As discussed previously, lowering the value of λ would increase the depth of the unstable layer, thereby producing this destabilising effect. These observations are also consistent with the results obtained by Veronis (1963). Furthermore, we also studied the influence of the Stefan number on the thermal instability mode, and found that this does not affect the critical Rayleigh number. This is qualitatively consistent with the results of Toppaladoddi & Wettlaufer (2019).

To understand the influence of Marangoni stresses on the thermal instability, we now solve the equations with $Ma > 0$. In figures 11(a) and 11(b), the dependence of Ra_c on Ma and k is shown, respectively. We see that an increase in Ma decreases the stability threshold. Hence, as noted by Nield (1964), the Marangoni stresses and the destabilising buoyancy forces act together to destabilise the system. Beyond a critical Marangoni number, Ra_c drops to zero. This is attributed to the thermocapillary instability becoming dominant. This is evident from the neutral curves shown figure 11(a). The switch from thermal to thermocapillary instability is seen to occur at $Ma \approx 550$, 450 and 430 for $d/h = 0$, 1 and 10 , respectively. The value $Ma = 500$ was chosen to highlight that $Ra_c = 0$ for $d/h = 1$ and 10 , but Ra_c is non-zero for $d/h = 0$. Therefore, the neutral curves corresponding to the thermocapillary and thermal modes (marked as ‘TC’ and ‘T’, respectively, in figure 11b) can be seen to be well separated for $d/h = 0$, but merged together for $d/h = 1$ and 10 . We also find that the stability threshold decreases further in the presence of an ice layer.

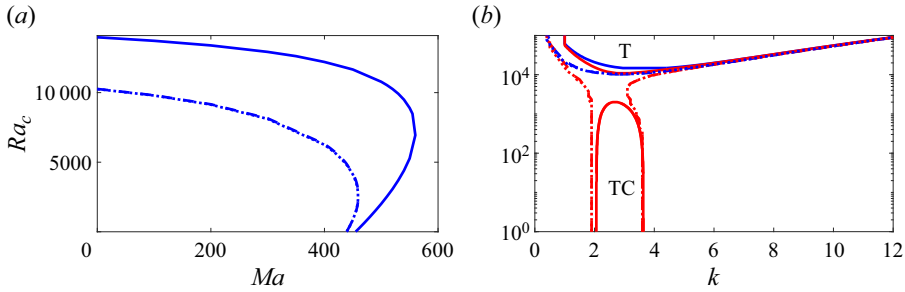


Figure 11. Neutral stability curve in (a) the Ra - Ma plane and (b) the Ra - k plane, for $d/h = 0$ (solid lines), $d/h = 1$ (dashed lines), $d/h = 10$ (dotted lines), $Ma = 0$ (blue lines) and $Ma = 500$ (red lines). In (b), ‘TC’ and ‘T’ denote the thermocapillary and thermal modes, respectively. The region outside the curves in (a) and inside the curves in (b) is the zone of instability.

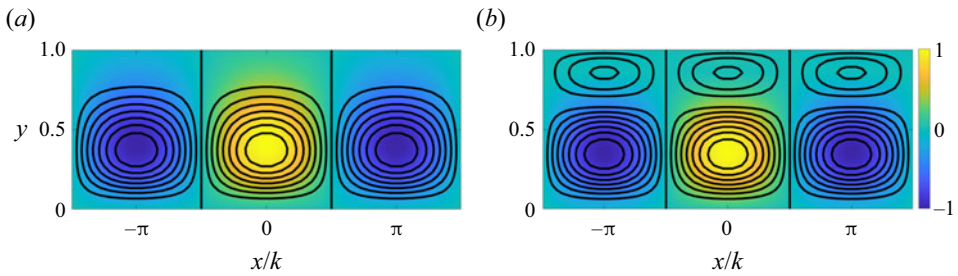


Figure 12. Perturbed temperature field with the streamfunction plotted for (a) $Ma = 0$ and (b) $Ma = 10^4$. The values of other parameters are $k = 3$, $Ra = 2 \times 10^4$ and $d/h = 0.1$.

The effects of the Marangoni stresses can also be seen in the temperature fields, which are shown in figure 12. In the absence of Marangoni stresses, we obtain the convection rolls set-up by the unstable stratification in the lower part of the fluid layer. However, for $Ma = 10^4$, we see additional rolls appearing near the free surface, indicating the onset of thermocapillary instability.

4. Conclusions

In this study, we explored the coupling between thermal and thermocapillary instabilities in a thin layer of liquid, and the impacts of an adjoining free liquid surface and a phase boundary on these instabilities. This was done by performing linear stability analysis on the Boussinesq equations with linear (Chandrasekhar 2013) and quadratic (Veronis 1963) equations of state for water.

We first explored the role of Marangoni stress, generated by surface-tension gradients, on the stability of the liquid layer. Since the inception of this instability is independent of thermal convection and is tractable analytically, we first studied the corresponding system using a linear equation of state. There are two possible types of thermocapillary instability – a stationary instability characterised by ‘steady convection rolls’, and an oscillatory instability (Takashima 1981b; Kalliadasis *et al.* 2011). Here, we focused solely on stationary thermocapillary instability except for a specific case to highlight the influence of the Stefan number. Consistent with the observations of Takashima (1981a), we found that Ma_c decreases with increasing wavenumber, and that it is independent of

the thickness of the ice layer for $k = O(1)$ and $k \gg 1$ (see [figure 4](#)). However, for $k \ll 1$, we find that Ma_c increases monotonically with d/h .

Next, in order to understand the effects of the unstably stratified layer on the thermocapillary instability, we included the nonlinear equation of state in the Boussinesq equations. Due to the analytical intractability of the resulting equations, we solved them numerically. The results obtained with the nonlinear equation of state were found to be qualitatively consistent with those obtained using the linear equation of state. However, for $k = O(1)$, the inclusion of the unstably stratified layer lowered the stability threshold significantly. We should note here that triggering the thermocapillary instability for $k \ll 1$ for an ice–water system is difficult (Rednikov *et al.* 2000). Hence this instability can appear only for $k \gg 1$ in an ice–water system.

After exploring the thermocapillary instability, we sought to understand the thermal instability in this system. This instability, as noted earlier, is due to the anomalous behaviour of water. We first studied the thermal instability by switching off the Marangoni stresses. Davis *et al.* (1984) had studied a similar system previously, albeit the working material being cyclohexane, with the solid layer overlying the liquid layer with no free surface. They observed that both Ra_c and k_c first decrease and then asymptote to constant values with increasing thickness of the solid layer. Our calculations revealed similar trends, thus highlighting the destabilising effect of the ice layer (see [figure 9](#)). We also found that an increase in Bi leads to an increase in Ra_c . This implies that the surface cooling has a stabilising effect on the system.

Finally, we calculated the stability thresholds over a range of Ma to ascertain the role of Marangoni stresses on the thermal instability. It is known that Marangoni stresses complement the buoyancy forces in driving the thermal instability (Nield 1964). We found that increasing Ma leads to a decrease in Ra_c (see [figure 11](#)), and that beyond a critical value of Ma , the thermocapillary instability takes over and destabilises the system independent of the value of Ra .

In the linear stability analysis of systems with moving boundaries, the deformations at these boundaries are assumed small and the relevant boundary conditions are linearised. This raises the question of what potential role these small deformations might play in determining the stability of the system. Takashima (1981a) studied the effect of the free-surface deformations on the stationary thermocapillary instability, and found that they were relevant only when $Ga < 120$. Such low Ga values correspond typically to the water layers of thickness less than 0.12 mm (Takashima 1981a; Velarde *et al.* 2001). Similar results were obtained by Regnier *et al.* (2000), who noted that the influence of surface deformations is bound to be minimal as long as liquid layers are of the order of 1 cm or higher in thickness, irrespective of the fluid's viscosity. The same conclusion can be drawn from the work by Lyubimov *et al.* (2018), who used a non-Boussinesq formulation to perform a linear stability analysis and showed that the capillary number should be $\gtrsim 8 \times 10^{-4}$ (corresponding to $\approx 3.5 \mu\text{m}$ thick water layer) for surface deformations to influence the stability characteristics. Similarly, previous linear stability studies in the literature have shown the lack of influence of the deformations of phase boundary on the marginal stability characteristics (Char & Chiang 1994).

In this idealised study, we have investigated the stability characteristics of the system by exploring the parameter space characterised by a set of relevant dimensionless numbers. However, in real systems, the control parameters are usually the free-surface temperature T_h , the thickness of the water layer h , and the thickness of the ice layer d . To relate our study to real systems, we perform a stability analysis by fixing the values of the constant physical parameters as listed in [table 1](#). [Figure 13](#) shows the contour map of the critical

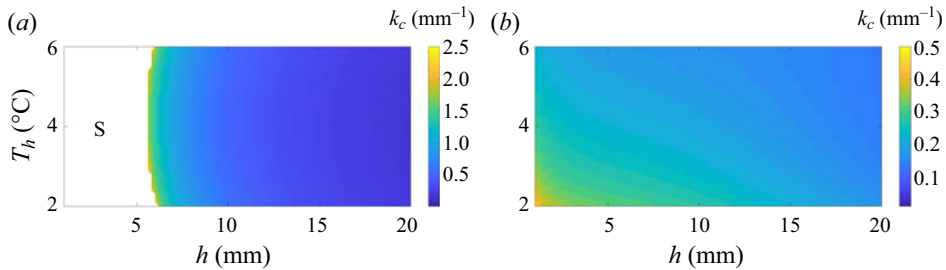


Figure 13. Contour plots (a) without surface-tension gradients, and (b) with surface-tension gradients, of the critical wavenumber in the T_h - h plane for an air–water–ice system with $d/h = 1$, where ‘S’ denotes the stable region. The inclusion of surface-tension gradients extends the region of instability and lowers the critical wavenumbers by triggering the thermocapillary mode of instability.

wavenumbers plotted in the T_h - h plane. When the surface-tension gradients are absent, the system can be destabilised solely by the thermal mode. In this case, we find that the water layer thickness must be $\gtrsim 5.6$ mm to trigger the thermal mode of instability. However, when the surface-tension gradient is included in the calculations, we find that the thermocapillary mode of instability destabilises the system in the entire explored range of parameters $T_h = 2$ – 6 °C and $h = 1$ – 20 mm at wavenumbers lower than the critical wavenumber associated with the thermal instability mode.



In § 1, we discussed the relevance of our study to the evolution of melt ponds. However, as noted earlier, the flow in a typical melt pond is confined in a non-uniform space, with large Ra , and is often saline, which can alter the melting temperature of ice (Eicken 1994; Lüthje *et al.* 2006; Gourdal *et al.* 2018; Kim *et al.* 2018). Previous studies in the literature have probed the effects of temperature and salt stratification (Carr 2003; Kim *et al.* 2018), and ice porosity (Hirata *et al.* 2012), sans a combination of a phase boundary and a free deformable interface. Nevertheless, this study provides a starting point for further investigation on the influence of these components, together with the wind forcing (Fetterer & Untersteiner 1998), on melt ponds and other fluid flows over phase boundaries in general.

In seeking to understand the effects of thermal and thermocapillary instabilities over a phase boundary, we have not included a mean flow. However, the presence of a mean flow has profound effects on both the stability and the morphology of the phase boundary (Gilpin *et al.* 1980; Meakin & Jamtveit 2010; Claudin, Durán & Andreotti 2017). The effect of a mean flow on the stability of such systems in bounded domains has been studied in different settings (Gilpin *et al.* 1980; Hindmarsh 2004; Shapiro & Timoshin 2006, 2007; Toppaladoddi & Wettlaufer 2019; Jiang *et al.* 2020; Satbhai & Roy 2020; Couston *et al.* 2021; Wang *et al.* 2021), but the effects of penetrative convection on free-surface flows in the presence of mean shear remains unexplored. Such a system could be susceptible to four different modes of instability – surface (long-wave interfacial instability), shear (short-wave, high-inertia instability), thermal (stemming from penetrative convection) and thermocapillary mode. The study of such a system will be a part of our future work.

Acknowledgements. D.J.D. and A.R. acknowledge support from IIT Madras through the ‘Geophysical Flows Lab’ research initiative under the Institute of Eminence framework. S.T. acknowledges a Research Fellowship from All Souls College, Oxford.

Declaration of interests. The authors report no conflict of interest.

Author ORCIDs.

-  Darish Jeswin Dhas <https://orcid.org/0000-0001-9766-8354>;
-  Anubhab Roy <https://orcid.org/0000-0002-0049-2653>;
-  S. Toppaladoddi <https://orcid.org/0000-0001-8450-2697>.

Appendix A. Thermocapillary instability – linear equation of state

With a linear equation of state, (3.4) and (3.14) become

$$\{Pr(\mathcal{D}^2 - k^2)^2 + ikc(\mathcal{D}^2 - k^2)\}\hat{v} - \{k^2 Ra Pr\}\hat{\theta}_l = 0, \tag{A1}$$

$$\begin{aligned} &\{ikc\mathcal{D} + Pr(\mathcal{D}^2 - 3k^2)\mathcal{D}\}\hat{v} \\ &- Pr k^2 \{Ra(\zeta^{-1} - \theta_l^b) + k^2[Ca^{-1} + Ma(\theta_l^b - \theta_h)]\}\hat{\eta}_2 = 0, \end{aligned} \tag{A2}$$

respectively, while the remaining set of equations remains the same. Since the density increases linearly with increasing temperature, $T_h = T_m$. After some algebra, (A1) and (3.5) are combined and written as

$$\left\{ Pr(\mathcal{D}^2 - k^2)^3 + (1 + Pr)ikc(\mathcal{D}^2 - k^2)^2 - k^2 c^2(\mathcal{D}^2 - k^2) - k^2 Ra Pr \frac{d\theta_l^b}{dy} \right\} \hat{v} = 0. \tag{A3}$$

Similarly, the boundary conditions become at $y = 0$

$$\mathcal{D}\hat{v} = 0, \tag{A4}$$

$$\hat{v} = 0, \tag{A5}$$

$$\{Pr(\mathcal{D}^2 - k^2)^2\mathcal{D} + ikc(\mathcal{D}^2 - k^2)\mathcal{D}\}\hat{v} - k^2 Ra Pr(\mathcal{D}\theta_s + ikcS\hat{\eta}_1) = 0, \tag{A6}$$

$$\eta_1 = -\frac{1 + Bi}{k^2 Ra Pr Bi} \{Pr(\mathcal{D}^4 - 2k^2\mathcal{D}^2 + k^4) + ikc(\mathcal{D}^2 - k^2)\}\hat{v}, \tag{A7}$$

and at $y = 1$

$$\{Pr(\mathcal{D}^2 - k^2)^2 + ikc(\mathcal{D}^2 - k^2) - \frac{Ra Pr}{Ma}(\mathcal{D}^2 + k^2)\}\hat{v} - k^2 Ra Pr \frac{Bi}{1 + Bi}\hat{\eta}_2 = 0, \tag{A8}$$

$$\begin{aligned} &\{ikc\mathcal{D} + Pr(\mathcal{D}^2 - 3k^2)\mathcal{D}\}\hat{v} \\ &- Pr k^2 \{Ra(\zeta^{-1} - \theta_l^b) + k^2[Ca^{-1} + Ma(\theta_l^b - \theta_h)]\}\hat{\eta}_2 = 0, \end{aligned} \tag{A9}$$

$$\begin{aligned} &\{Pr((\mathcal{D}^2 - k^2)^2\mathcal{D} + Bi(\mathcal{D}^2 - k^2)^2) + ikc(\mathcal{D}^2 - k^2)(\mathcal{D} + Bi)\}\hat{v} \\ &+ k^2 Ra Pr \frac{Bi^2}{1 + Bi}\hat{\eta}_2 = 0, \end{aligned} \tag{A10}$$

$$ikc\hat{\eta}_2 + \hat{v} = 0. \tag{A11}$$

The solution to the above system of equations sought in the form $\sim C_i \exp(\lambda_i y)$ is

$$\hat{v}(s, y) = \sum_{i=1}^6 \exp(\lambda_i y) C_i(s), \tag{A12}$$

where $s = ikc$, C_i are constants, and λ_i are the eigenvalues. Substituting (A12) in boundary conditions (A4)–(A11), we obtain a dispersion matrix. Since we are interested in the marginal states of the stationary thermocapillary mode, we set $c = 0$ and subsequently calculate the critical value of the Marangoni number.

Appendix B. Numerical method for solving the linear stability equations

Equations (3.4)–(3.16) are solved numerically for the eigenvalue c using a spectral collocation method. For this, we first use Lagrange polynomials to approximate the solution for \hat{v} , $\hat{\theta}_l$ and $\hat{\theta}_s$, and discretise the physical domain using Chebyshev grid points (Trefethen 2000):

$$\hat{v} = \sum_{j=0}^{N-1} L_{ij} \hat{v}_j, \quad \hat{\theta}_l = \sum_{j=0}^{N-1} L_{ij} \hat{\theta}_{lj}, \quad \hat{\theta}_s = \sum_{j=0}^{N-1} L_{ij} \hat{\theta}_{sj}, \quad c = \sum_{j=0}^{N-1} L_{ij} c_j. \quad (\text{B1a-d})$$

Here, \hat{v}_j , $\hat{\theta}_{lj}$, $\hat{\theta}_{sj}$ and c_j are \hat{v} , $\hat{\theta}_l$, $\hat{\theta}_s$ and c at Chebyshev grid points $z_j = \cos(j\pi/N)$, and N is the number of collocation points used to discretise the domain. The Chebyshev grid points lie in the interval $[-1, 1]$, whereas in the physical domain of the problem, the fluid phase lies in the interval $[0, 1]$ and the solid phase lies in the interval $[-d/h, 0]$. Therefore, we map the Chebyshev grid points to the domains $[0, 1]$ and $[-d/h, 0]$ using the relation $y_j = 0.5(1 - z_j)$ and $y_j = -0.5d/h(1 + z_j)$. The resulting system can be written in the form of a generalised eigenvalue problem as

$$\mathbf{A} \cdot \mathbf{q} = c \mathbf{B} \cdot \mathbf{q}, \quad (\text{B2})$$

where $\mathbf{q} = \{\hat{v}_j, \hat{\theta}_{lj}, \hat{\theta}_{sj}, \hat{\eta}_1, \hat{\eta}_2\}$, and \mathbf{A} and \mathbf{B} are matrices of order $3N + 5$. We then proceed to solve the above eigenvalue problem using the MATLAB subroutine eig. To obtain converged solutions, we begin with $N = 30$, and increase N until the eigenspectrum converges. We find that the converged eigenspectrum is obtained typically at $N \approx 40$.

REFERENCES

- BUSHUK, M., HOLLAND, D.M., STANTON, T.P., STERN, A. & GRAY, C. 2019 Ice scallops: a laboratory investigation of the ice–water interface. *J. Fluid Mech.* **873**, 942–976.
- CAMPORALE, C. & RIDOLFI, L. 2012 Ice ripple formation at large Reynolds numbers. *J. Fluid Mech.* **694**, 225–251.
- CAMPORALE, C., VESIPA, R. & RIDOLFI, L. 2017 Convective-absolute nature of ripple instabilities on ice and icicles. *Phys. Rev. Fluids* **2** (5), 053904.
- CARR, M. 2003 A model for convection in the evolution of under-ice melt ponds. *Contin. Mech. Thermodyn.* **15**, 45–54.
- CHANDRASEKHAR, S. 2013 *Hydrodynamic and Hydromagnetic Stability*. Courier Corporation.
- CHAR, M.I. & CHIANG, K.T. 1994 Morphological instability on Bénard–Marangoni convection during solidification: single-component system. *Intl J. Heat Mass Transfer* **37** (13), 1935–1943.
- CLAUDIN, P., DURÁN, O. & ANDREOTTI, B. 2017 Dissolution instability and roughening transition. *J. Fluid Mech.* **832**, R2.
- CORIELL, S.R., MCFADDEN, G.B., BOISVERT, R.F. & SEKERKA, R.F. 1984 Effect of a forced Couette flow on coupled convective and morphological instabilities during unidirectional solidification. *J. Cryst. Growth* **69** (1), 15–22.
- COUSTON, L.A., HESTER, E., FAVIER, B., TAYLOR, J.R., HOLLAND, P.R. & JENKINS, A. 2021 Topography generation by melting and freezing in a turbulent shear flow. *J. Fluid Mech.* **911**, A44.
- DAVIS, S.H., MÜLLER, U. & DIETSCHKE, C. 1984 Pattern selection in single-component systems coupling Bénard convection and solidification. *J. Fluid Mech.* **144**, 133–151.
- DEGUEN, R., ALBOUSSIÈRE, T. & CARDIN, P. 2013 Thermal convection in Earth’s inner core with phase change at its boundary. *Geophys. J. Intl* **194** (3), 1310–1334.
- DELVES, R.T. 1968 Theory of stability of a solid–liquid interface during growth from stirred melts. *J. Cryst. Growth* **3**, 562–568.
- DELVES, R.T. 1971 Theory of the stability of a solid–liquid interface during growth from stirred melts II. *J. Cryst. Growth* **8** (1), 13–25.
- DHAS, D.J. & ROY, A. 2022 Stability of gravity-driven particle-laden flows – roles of shear-induced migration and normal stresses. *J. Fluid Mech.* **938**, A29.

- DIETSCHKE, C. & MÜLLER, U. 1985 Influence of Bénard convection on solid–liquid interfaces. *J. Fluid Mech.* **161**, 249–268.
- EICKEN, H. 1994 Structure of under-ice melt ponds in the central Arctic and their effect on the sea-ice cover. *Limnol. Oceanogr.* **39** (3), 682–693.
- ESFAHANI, B.R., HIRATA, S.C., BERTI, S. & CALZAVARINI, E. 2018 Basal melting driven by turbulent thermal convection. *Phys. Rev. Fluids* **3** (5), 053501.
- FAVIER, B., PURSEED, J. & DUCHEMIN, L. 2019 Rayleigh–Bénard convection with a melting boundary. *J. Fluid Mech.* **858**, 437–473.
- FELTHAM, D.L. & WORSTER, M.G. 1999 Flow-induced morphological instability of a mushy layer. *J. Fluid Mech.* **391**, 337–357.
- FETTERER, F. & UNTERSTEINER, N. 1998 Observations of melt ponds on Arctic sea ice. *J. Geophys. Res.* **103** (C11), 24821–24835.
- FORTH, S.A. & WHEELER, A.A. 1989 Hydrodynamic and morphological stability of the unidirectional solidification of a freezing binary alloy: a simple model. *J. Fluid Mech.* **202**, 339–366.
- GILPIN, R.R., HIRATA, T. & CHENG, K.C. 1980 Wave formation and heat transfer at an ice–water interface in the presence of a turbulent flow. *J. Fluid Mech.* **99** (3), 619–640.
- GOURDAL, M., LIZOTTE, M., MASSÉ, G., GOSSELIN, M., POULIN, M., SCARRATT, M., CHARETTE, J. & LEVASSEUR, M. 2018 Dimethyl sulfide dynamics in first-year sea ice melt ponds in the Canadian Arctic archipelago. *Biogeosciences* **15** (10), 3169–3188.
- HEWITT, I.J. 2020 Subglacial plumes. *Annu. Rev. Fluid Mech.* **52**, 145–169.
- HINDMARSH, R.C.A. 2004 Thermoviscous stability of ice-sheet flows. *J. Fluid Mech.* **502**, 17–40.
- HIRATA, S.C., GOYEAU, B. & GOBIN, D. 2012 Onset of convective instabilities in under-ice melt ponds. *Phys. Rev. E* **85** (6), 066306.
- HITCHEN, J. & WELLS, A.J. 2016 The impact of imperfect heat transfer on the convective instability of a thermal boundary layer in a porous media. *J. Fluid Mech.* **794**, 154–174.
- HUPPERT, H.E. 1990 The fluid mechanics of solidification. *J. Fluid Mech.* **212**, 209–240.
- JIANG, L.Y., CHENG, Z. & PENG, J. 2020 Water film falling down an ice sheet. *J. Fluid Mech.* **896**, A3.
- KALLIADASIS, S., RUYER-QUIL, C., SCHEID, B. & VELARDE, M.G. 2011 *Falling Liquid Films*, vol. 176. Springer Science & Business Media.
- KIM, J.H., MOON, W., WELLS, A.J., WILKINSON, J.P., LANGTON, T., HWANG, B., GRANSKOG, M.A. & REES JONES, D.W. 2018 Salinity control of thermal evolution of late summer melt ponds on Arctic sea ice. *Geophys. Res. Lett.* **45** (16), 8304–8313.
- KURZ, W. & FISHER, D.J. 1984 *Fundamentals of Solidification*. Trans Tech Publications.
- LÜTHJE, M., FELTHAM, D.L., TAYLOR, P.D. & WORSTER, M.G. 2006 Modeling the summertime evolution of sea-ice melt ponds. *J. Geophys. Res.* **111** (C2), C02001.
- LYUBIMOV, D.V., LYUBIMOVA, T.P., LOBOV, N.I. & ALEXANDER, J.I.D. 2018 Rayleigh–Bénard–Marangoni convection in a weakly non-Boussinesq fluid layer with a deformable surface. *Phys. Fluids* **30** (2), 024103.
- MAKKONEN, L. 1988 A model of icicle growth. *J. Glaciol.* **34** (116), 64–70.
- MASLOWSKI, W., CLEMENT KINNEY, J., HIGGINS, M. & ROBERTS, A. 2012 The future of Arctic sea ice. *Annu. Rev. Earth Planet. Sci.* **40**, 625–654.
- MAYKUT, G.A. & PEROVICH, D.K. 1987 The role of shortwave radiation in the summer decay of a sea ice cover. *J. Geophys. Res.* **92** (C7), 7032–7044.
- MCPHEE, M.G. 2008 *Air–Ice–Ocean Interaction: Turbulent Ocean Boundary Layer Exchange Processes*. Springer Science & Business Media.
- MEAKIN, P. & JAMTVEIT, B. 2010 Geological pattern formation by growth and dissolution in aqueous systems. *Proc. R. Soc. A* **466** (2115), 659–694.
- NEUFELD, J.A. & WETTTLAUFER, J.S. 2008a An experimental study of shear-enhanced convection in a mushy layer. *J. Fluid Mech.* **612**, 363–385.
- NEUFELD, J.A. & WETTTLAUFER, J.S. 2008b Shear-enhanced convection in a mushy layer. *J. Fluid Mech.* **612**, 339–361.
- NIELD, D.A. 1964 Surface tension and buoyancy effects in cellular convection. *J. Fluid Mech.* **19** (3), 341–352.
- OGAWA, N. & FURUKAWA, Y. 2002 Surface instability of icicles. *Phys. Rev. E* **66** (4), 041202.
- PURSEED, J., FAVIER, B., DUCHEMIN, L. & HESTER, E.W. 2020 Bistability in Rayleigh–Bénard convection with a melting boundary. *Phys. Rev. Fluids* **5** (2), 023501.
- RAMUDU, E., HIRSH, B.H., OLSON, P. & GNANADESIKAN, A. 2016 Turbulent heat exchange between water and ice at an evolving ice–water interface. *J. Fluid Mech.* **798**, 572–597.
- RAVICHANDRAN, S. & WETTTLAUFER, J.S. 2021 Melting driven by rotating Rayleigh–Bénard convection. *J. Fluid Mech.* **916**, A28.

- REDNIKOV, A.Y., COLINET, P., VELARDE, M.G. & LEGROS, J.C. 2000 Rayleigh–Marangoni oscillatory instability in a horizontal liquid layer heated from above: coupling and mode mixing of internal and surface dilational waves. *J. Fluid Mech.* **405**, 57–77.
- REGNIER, V.C., DAUBY, P.C. & LEBON, G. 2000 Linear and nonlinear Rayleigh–Bénard–Marangoni instability with surface deformations. *Phys. Fluids* **12** (11), 2787–2799.
- SATBHAI, O. & ROY, S. 2020 Criteria for the onset of convection in the phase-change Rayleigh–Bénard system with moving melting-boundary. *Phys. Fluids* **32** (6), 064107.
- SHAPIRO, E. & TIMOSHIN, S. 2006 Linear stability of ice growth under a gravity-driven water film. *Phys. Fluids* **18** (7), 074106.
- SHAPIRO, E. & TIMOSHIN, S. 2007 On ice-induced instability in free-surface flows. *J. Fluid Mech.* **577**, 25–52.
- SHORT, M.B., BAYGENTS, J.C., BECK, J.W., STONE, D.A., TOOMEY III, R.S. & GOLDSTEIN, R.E. 2005a Stalactite growth as a free-boundary problem: a geometric law and its Platonic ideal. *Phys. Rev. Lett.* **94** (1), 018501.
- SHORT, M.B., BAYGENTS, J.C. & GOLDSTEIN, R.E. 2005b Stalactite growth as a free-boundary problem. *Phys. Fluids* **17** (8), 083101.
- SHORT, M.B., BAYGENTS, J.C. & GOLDSTEIN, R.E. 2006 A free-boundary theory for the shape of the ideal dripping icicle. *Phys. Fluids* **18** (8), 083101.
- SKYLLINGSTAD, E.D. & PAULSON, C.A. 2007 A numerical study of melt ponds. *J. Geophys. Res.* **112** (C8), C08015.
- SODERLUND, K.M., *et al.* 2020 Ice–ocean exchange processes in the Jovian and Saturnian satellites. *Space Sci. Rev.* **216** (5), 1–57.
- SZILDER, K. & LOZOWSKI, E.P. 1994 An analytical model of icicle growth. *Ann. Glaciol.* **19**, 141–145.
- TAKASHIMA, M. 1981a Surface tension driven instability in a horizontal liquid layer with a deformable free surface. I. Stationary convection. *J. Phys. Soc. Japan* **50** (8), 2745–2750.
- TAKASHIMA, M. 1981b Surface tension driven instability in a horizontal liquid layer with a deformable free surface. II. Overstability. *J. Phys. Soc. Japan* **50** (8), 2751–2756.
- TAYLOR, P.D. & FELTHAM, D.L. 2004 A model of melt pond evolution on sea ice. *J. Geophys. Res.* **109** (C12), C12007.
- TOPPALADODDI, S. 2021 Nonlinear interactions between an unstably stratified shear flow and a phase boundary. *J. Fluid Mech.* **919**, A28.
- TOPPALADODDI, S. & WETTLAUFER, J.S. 2018 Penetrative convection at high Rayleigh numbers. *Phys. Rev. Fluids* **3** (4), 043501.
- TOPPALADODDI, S. & WETTLAUFER, J.S. 2019 The combined effects of shear and buoyancy on phase boundary stability. *J. Fluid Mech.* **868**, 648–665.
- TREFETHEN, L.N. 2000 *Spectral Methods in MATLAB*. SIAM.
- UENO, K. 2007 Ripples on icicles and stalactites. *RIMS Kôkyûroku Bessatsu B* **3**, 101–119.
- VELARDE, M.G., NEPOMNYASHCHY, A.A. & HENNENBERG, M. 2001 Onset of oscillatory interfacial instability and wave motions in Bénard layers. *Adv. Appl. Mech.* **37**, 167–238.
- VERONIS, G. 1963 Penetrative convection. *Astrophys. J.* **137**, 641.
- WALKER, C.C. & SCHMIDT, B.E. 2015 Ice collapse over trapped water bodies on Enceladus and Europa. *Geophys. Res. Lett.* **42** (3), 712–719.
- WANG, Z., CALZAVARINI, E., SUN, C. & TOSCHI, F. 2021 How the growth of ice depends on the fluid dynamics underneath. *Proc. Natl Acad. Sci. USA* **118** (10), e2012870118.
- WETTLAUFER, J.S. & WORSTER, M.G. 2006 Premelting dynamics. *Annu. Rev. Fluid Mech.* **38** (1), 427–452.
- WETTLAUFER, J.S., WORSTER, M.G. & HUPPERT, H.E. 1997 Natural convection during solidification of an alloy from above with application to the evolution of sea ice. *J. Fluid Mech.* **344**, 291–316.
- WORSTER, M.G. 1997 Convection in mushy layers. *Annu. Rev. Fluid Mech.* **29** (1), 91–122.
- WYKES, M.S.D., HUANG, M.J., HAJJAR, G.A. & RISTROPH, L. 2018 Self-sculpting of a dissolvable body due to gravitational convection. *Phys. Rev. Fluids* **3** (4), 043801.
- YIH, C.S. 1963 Stability of liquid flow down an inclined plane. *Phys. Fluids* **6** (3), 321–334.